Homogeneous nucleation in supersaturated vapors of real fluids predicted by brute force molecular dynamics

Martin Horsch[†], Jadran Vrabec[*†], Martin Bernreuther[‡], Sebastian Grottel[§], Guido Reina[§], Andrea Wix[¶], Karlheinz Schaber[¶], and Hans Hasse[†]

Abstract

Molecular dynamics (MD) simulation is applied to the condensation process of supersaturated vapors of methane, ethane, and carbon dioxide. By using a massively parallel MD program, simulations of systems with a million particles become feasible with an acceptable effort. This leads to reliable statistics and makes a large range of nucleation rates accessible to the direct simulation approach. Simulation results are compared to the classical nucleation theory (CNT) as well as the theory proposed by Laaksonen, Ford, and Kulmala (LFK) which introduces a size dependence of the specific surface energy. CNT describes the nucleation of ethane and carbon dioxide accurately, whereas LFK provides a better approach to some systems at low temperatures. Deviations of three orders of magnitude from simulation results are observed for both theories.

1 Introduction

Homogeneous nucleation was discussed theoretically by Gibbs [1] and studied in depth by Volmer and Weber [2] as well as Farkas [3]. In combination with experiments carried out by Wilson [4] and Powell [5] during the same period, these efforts established the classical nucleation theory (CNT), which is known to be accurate in many cases but to fail in others [6, 7, 8].

Molecular simulations are applied to this problem since the late 1950s, when Alder and Wainwright [9] observed a first-order phase transition in molecular dynamics (MD) simulations of the hard sphere fluid. In the 1970s, McGinty [10] studied liquid clusters of the Lennard-Jones (LJ) fluid in MD simulations, and Rao et al. [11] described the condensation of a supersaturated vapor with results obtained from both Monte Carlo (MC) and MD simulations. Some common approaches to the dynamics of nucleation, such as MD simulations with inserted droplets [12, 13, 14, 15, 16] or transition path sampling [17, 18, 19] as well as MC simulations [19, 20, 21, 22, 23], do not lead immediately to the velocity of the phase transition, but only to *indirect* information, e.g. on the required activation energy. The present study discusses brute force MD simulations, which are aimed at the *direct* reproduction of a nucleation process by means of the deterministic simulation of a large system.

Nucleation processes are characterized by the nucleation rate J, i.e. the number of stable liquid nuclei generated per volume and time, and their critical size ι^*, i.e. the number of molecules in a nucleus with maximal Gibbs energy of formation. Droplets above that size have a higher probability to further grow, whereas smaller clusters tend to evaporate. Due to current limitations in the available computational resources, only nucleation processes with extremely large values of J can be simulated by MD. However, when nucleation occurs very rapidly, the vapor phase is not fully in equilibrium with the emerging droplets and the critical size is not constant. It is nonetheless possible to determine nucleation rates if one follows the somewhat heuristic approach proposed by Yasuoka and Matsumoto [24]. Most recent direct MD studies of nucleation [25, 26, 27, 28] adhere to this method.

The method of Yasuoka and Matsumoto requires system sizes and simulation times to be as large as possible. Due to restrictions of computational power, the lowest nucleation rates which can be obtained nowadays with this approach – above $10^{30}/(\mathrm{m}^3\mathrm{s})$ in the present study – exceed those which actually can be observed in experiments by about seven orders of magnitude [29]. This gap can only be closed by predictions on the basis of nucleation theories that express the dependence of J and ι^* on temperature and pressure, where the latter is often given in terms of the supersaturation $\mathcal{S}_p(p,T) = p/p_\sigma(T)$, i.e. related to the vapor pressure p_σ. Reviews following the progress of the last decades are provided by Oxtoby [30, 31] and Ford [8]. For a description of advanced experimental methods see also Fladerer and Strey [32] as well as Iland [29].

In the following sections, CNT and a version of the Dillmann-Meier [33] model due to Laaksonen, Ford, and Kulmala [34], referred to as LFK here, will be discussed and compared to data from direct MD simulations. It is also necessary to comment on the *mean first passage time* (MFPT) approach, an indirect method which fits a predefined kinetic model with three parameters to simulation results [35, 36].

*Corresponding author. E-mail: vrabec@itt.uni-stuttgart.de
†Universität Stuttgart, Institute of Thermodynamics and Thermal Process Engineering, Pfaffenwaldring 9, 70569 Stuttgart, Germany
‡High Performance Computing Center Stuttgart, Nobelstr. 19, 70550 Stuttgart, Germany
§Universität Stuttgart, Institute of Visualization and Interactive Systems, Universitätsstr. 38, 70569 Stuttgart, Germany
¶Universität Karlsruhe, Institut für Technische Thermodynamik und Kältetechnik, Engler-Bunte-Ring 21, 76131 Karlsruhe, Germany

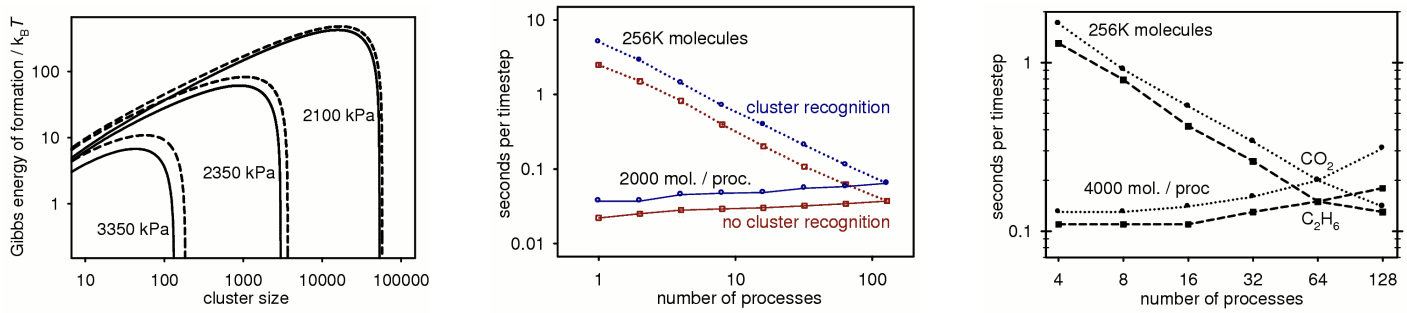

Figure 1: **left** – Gibbs energy of cluster formation in CO_2 at 253 K for pressure values of 2100, 2350, and 3350 kPa according to CNT (—) and LFK (- - -); **center** – Strong (256000 molecules) and weak scaling (2000 molecules per process) of $\mathbf{ls}_1$ simulating CH_4 at 102 K and 0.730 mol/l on the Intel Xeon cluster *mozart* at the chairs *Simulation of Large Systems* and *Numerics for Supercomputers*, Universität Stuttgart; **right** – Strong (256000 molecules) and weak scaling (4000 molecules per process) of $\mathbf{ls}_1$ for 2CLJQ fluid models on the Intel Xeon cluster *cacau* at the *High Performance Computing Center Stuttgart*: C_2H_6 at 183 K and 0.365 mol/l (- - -) as well as CO_2 at 253 K and 1.670 mol/l ($\cdots$)

2 Nucleation theories

2.1 Classical nucleation theory

The foundations of CNT were laid by Gibbs [1] and further developed by Volmer and Weber [2]. Important subsequent contributions were made by Farkas [3], Becker and Döring [37], Zel'dovich [38], and Feder et al. [39]. For the further development of the theory compare Kashchiev [40] and Vehkamäki [41].

The starting point of this theory is the capillarity approximation: the dispersed liquid phase, composed of the clusters emerging during nucleation, is assumed to have the same thermodynamic properties as the saturated bulk liquid. It is also assumed that all liquid clusters are spherical. CNT describes how, under such preconditions, nucleation rate and critical size depend on temperature, supersaturation, and a few properties of the fluid which are independent of $\mathcal{S}_p$, such as the planar interface surface tension γ_0 and the densities ρ_σ and ρ_ι, referring to the saturated vapor and liquid, repsectively.

The surface energy $\phi(\iota)$ of a cluster with ι molecules, the surface area $A(\iota)$, and the specific surface energy $\mathcal{E}$ amounts to $\mathcal{E}A(\iota)$. The capillarity approximation assigns $\mathcal{E} = \gamma_0$, and CNT further assumes spherical clusters, hence $A(\iota) = \sqrt[3]{\pi}\,(6\iota/\rho_\iota)^{2/3}$. The Gibbs energy of cluster formation in a supersaturated vapor consists of a negative bulk contribution and a positive surface contribution [1, 2]. It amounts to

$$\Delta G_\iota \;=\; \phi(\iota) - \phi(1) + (1-\iota)\Delta\mu, \tag{1}$$

and reaches a maximum at the size ι^* of the critical nucleus. It can be seen from Figure 1 (left) that the critical size is strongly dependent on the supersaturated vapor pressure; it diverges as the supersaturated vapor pressure p approaches the saturated vapor pressure p_σ of the bulk fluid. The chemical potential difference,

$$\Delta\mu \;=\; \int_{p_\sigma}^{p} dp/\rho_{\mathrm{v}}, \tag{2}$$

is an integral between p_σ and p at constant temperature. In metastable equilibrium, the ι-cluster number density $\rho_\iota = N_\iota/V$, where N_ι is the number of clusters with exactly ι molecules, amounts to

$$\rho_\iota \;=\; \rho_1 \exp\left(\frac{-\Delta G_\iota}{kT}\right), \tag{3}$$

where ρ_1 can be estimated from

$$\rho \;\simeq\; \sum_{\iota=1}^{\iota^*} \iota\rho_\iota. \tag{4}$$

The impact rate β of vapor molecules on a cluster per surface area can be approximated by

$$\beta \;=\; \frac{p}{\sqrt{2\pi mkT}}, \tag{5}$$

where m is the molecular mass [42]. Assuming that every collision of a monomer with a critical nucleus leads to the formation of a cluster with $1+\iota^*$ molecules, the nucleation rate is given by

$$J \;=\; \rho^*\beta A^*\mathcal{Z}\vartheta. \tag{6}$$

Here and elsewhere, all quantities marked with an asterisk refer to critical nuclei. The factor βA^* expresses the impact frequency of monomers on a critical nucleus, or equivalently, the rate at which critical nuclei grow to a size of $1+\iota^*$ molecules.

The two remaining factors, $\mathcal{Z}$ and ϑ, represent corrections with respect to the nucleus density, the kinetics of the nucleation process, and the temperature inside a nucleus. The metastable equilibrium breaks down near the critical size, and the actual number density of critical nuclei is considerably lower than their metastable equilibrium density ρ^*. The Zel'dovich factor,

$$\mathcal{Z} \;=\; \sqrt{\frac{-1}{2\pi kT}\left(\frac{\partial^2 G_\iota}{\partial\iota^2}\right)_{\iota^*}} \;=\; \frac{1}{3\iota^*}\sqrt{\frac{\phi^*}{\pi kT}}, \tag{7}$$

takes into account both this difference and the probability that that a nucleus above the critical size does not continue to grow [38].

Nuclei which reach the critical size usually have grown very fast and retain part of the latent heat. This increase in temperature reduces the nucleation rate, an effect which is quantified by the non-isothermal factor ϑ introduced by Feder et al. [39]. Let c_v be the isochoric heat capacity of the vapor, and ΔH_v the enthalpy of evaporation. The excess energy, added to a critical nucleus when it consumes a monomer above what is needed to maintain the temperature and to extend the surface area, amounts to

$$q \;=\; \Delta H_v - \frac{kT}{2} - \left(\frac{\partial \phi(\iota)}{\partial \iota}\right)_{\iota^*} \;=\; \Delta H_v - \frac{kT}{2} - \frac{2\phi^*}{3\iota^*}. \quad (8)$$

The standard deviation of the energy of vapor molecules that collide with a cluster is

$$b \;=\; T\sqrt{k(c_v + k/2)}. \quad (9)$$

Finally, the non-isothermal factor is given by

$$\vartheta \;=\; \frac{b^2}{b^2 + q^2}. \quad (10)$$

2.2 Model proposed by Laaksonen, Ford, and Kulmala

The LFK model [34] is a version of the Dillmann-Meier approach [33] which postulates the surface energy of a cluster with $\iota \in \mathbb{N}$ molecules to be

$$\phi(\iota) \;=\; \kappa(\iota)\gamma_0 A(\iota) + \tau kT \ln \iota. \quad (11)$$

The adjustable parameters of this model are τ and $\kappa(\iota)$ for $\iota \in \mathbb{N}$, as well as ρ_1 which is expressed indirectly by means of a normalization parameter q_0. By comparing the Fisher [43] equation of state,

$$p \;=\; kT \sum_{\iota \in \mathbb{N}} \rho_\iota, \quad (12)$$

to a virial-type expansion of second order values for $\kappa(1)$ and $\kappa(2)$ are defined. Laaksonen et al. [34] represent this in terms of the monomer density as

$$\rho_1 \;=\; \frac{p}{kT}\left(1 + \frac{\mathcal{B}p}{kT}\right) \;=\; \frac{p^2}{\rho (kT)^2}, \quad (13)$$

where the second virial coefficient is, in this case, defined as

$$\mathcal{B} \;=\; \rho^{-1} - p^{-1}kT. \quad (14)$$

They obtain the expressions

$$\begin{aligned} \kappa(1) &= -\frac{1}{\Theta}\left(\ln\left(\frac{p_\sigma}{q_0 kT}\right) + \frac{\mathcal{B}p_\sigma}{kT}\right), \\ \kappa(2) &= -\frac{1}{\Theta 2^{2/3}}\left(\frac{\mathcal{B}p_\sigma}{kT} - \kappa(1)\Theta + \ln\left(\frac{-2^\tau \mathcal{B}p_\sigma}{kT}\right)\right), \end{aligned}$$

with $\Theta = \gamma_0 A(1)/kT$, by applying an approximation to Equation (4). This is extended to higher $\kappa(\iota)$ by

$$\kappa(\iota) \;=\; 1 + \alpha_1 \iota^{-1/3} + \alpha_2 \iota^{-2/3}, \quad (15)$$

which are the first three contributions of an expansion in terms of the inverse cluster radius $r^{-1} \sim \iota^{-1/3}$. The coefficients α_1 and α_2 are determined by equating the expressions for $\kappa(1)$ and $\kappa(2)$ with Equation (15).

Note that since Equation (11) multiplies $\kappa(\iota)$ with $A(\iota) \sim \iota^{2/3}$, the value of α_2 only influences a constant summand which cancels out in the expression for ΔG_ι. Laaksonen et al. [34] proposed $\tau = 0$, and Ford et al. [44] showed that with this particular assignment, the parameter q_0 cancels out as well. To obtain a convenient expression, we set $q_0 = p_\sigma/kT$, which leads to

$$\kappa(1) \;=\; \frac{-\mathcal{B}p_\sigma}{\gamma_0 A(1)}, \quad (16)$$

$$\kappa(2) \;=\; \frac{-2\mathcal{B}p_\sigma - kT\ln(-\mathcal{B}p_\sigma/kT)}{\gamma_0 A(2)}. \quad (17)$$

The Zel'dovich factor takes the form

$$\mathcal{Z} \;=\; \frac{1}{3\iota^*}\sqrt{\frac{\gamma_0 A(1)}{\pi kT}\sqrt[3]{\iota^*}\left(\alpha_1 + \sqrt[3]{\iota^*}\right)}, \quad (18)$$

and the energy released on addition of a monomer to a cluster amounts to

$$q \;=\; \Delta H_v - \frac{kT}{2} - \frac{\gamma_0 A(1)}{3\sqrt[3]{\iota}}\left(2 + \frac{\alpha_1}{\sqrt[3]{\iota}}\right). \quad (19)$$

Compared to CNT, the LFK model hence introduces a size dependence of the specific surface energy which is governed by the single parameter α_1. Figure 1 (left) illustrates that this size dependence becomes particularly significant at high supersaturations, where the critical nucleus is small.

2.3 Mean first passage times

Let us next consider the kinetics of a nucleation process. For a supersaturated fluid in a volume V that exhibits the nucleation rate J, it might be expected that the first stable nuclei appear on average after a temporal delay, expressed by

$$\mathit{\Gamma}(\iota) \;\approx\; \frac{1}{JV}, \quad (20)$$

for some $\iota > \iota^*$, after the onset of nucleation [45]. The average delay $\mathit{\Gamma}(\iota)$ until the first cluster with ι molecules appears is called the *mean first passage time* of ι. Wedekind et al. [36, 46, 47] generalized this approach to a theory of condensation processes, here referred to as MFPT. Bartell and Wu [35] obtained an identical result for freezing, and Zhang et al. [48] applied it to melting processes. According to this approach, the mean first passage time is approximated using a Gauss error function,

$$\mathit{\Gamma}(\iota) \;=\; \frac{\mathit{\Gamma}_\infty}{2}\left[\,1 + \mathrm{erf}(\,x(\iota - \iota^*)\,)\,\right]. \quad (21)$$

In particular, this approach leads to

$$\lim_{\iota \to \infty} \mathit{\Gamma}(\iota) \;=\; \mathit{\Gamma}_\infty \;=\; 2\mathit{\Gamma}^*, \quad (22)$$

and thus

$$J \;\approx\; \frac{1}{2\mathit{\Gamma}^* V}, \quad (23)$$

from Equation (20) with $\iota \to \infty$ [45]. These approximations are intended to hold only 'in the vicinity of the critical size' and '[u]nder reasonably high barriers' [36].

	model	m [u]	σ [Å]	ϵ [$k \times$ K]	Q [B]	L [Å]
CH_4	LJ	16.04	3.7281	148.55		
C_2H_6	2CLJQ	2×15.03	3.4896	136.99	0.8277	2.3762
CO_2	2CLJQ	2×22.00	2.9847	133.22	3.7938	2.4176

Table 1: Parameters of the molecular models for methane, ethane, and carbon dioxide

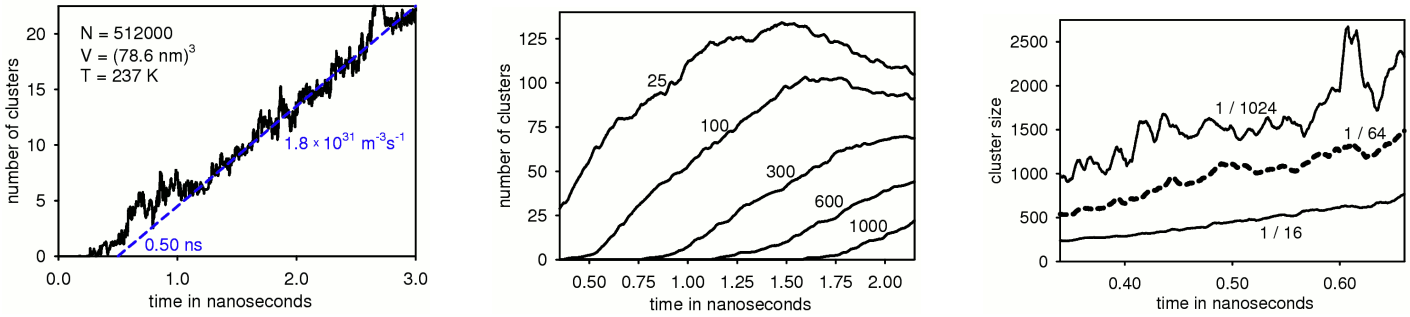

Figure 2: **left** – Number of nuclei containing at least 75 molecules in supersaturated CO_2 vapor over simulation time; **center** – Number of nuclei containing at least 25, 100, ..., 1000 molecules over simulation time in $(63.7\text{ nm})^3$ filled with methane at 130 K and 1.606 mol/l; **right** – Cluster formation delay $\nu_x(t)$ for CO_2 at 253 K and 3.150 mol/l with $N = 884700$ and $x \in \{2^{-4}, 2^{-6}, 2^{-10}\}$.

3 Simulation method

Methane, ethane and carbon dioxide were selected in the present work because of their qualitatively different molecular properties. Methane is almost spherical and weakly octupolar, thus it can be described by a single Lennard-Jones site with the pair potential

$$u_{\mathrm{LJ}}(r_{ij}) \;=\; 4\epsilon \left(\left(\frac{\sigma}{r_{ij}}\right)^{12} - \left(\frac{\sigma}{r_{ij}}\right)^{6} \right). \qquad (24)$$

Ethane molecules are dumbbell-shaped and thus significantly anisotropic in geometry but only slightly quadrupolar. Carbon dioxide molecules are both strongly anisotropic and quadrupolar. The intermolecular interactions of these two fluids were described by the two-center LJ model with an embedded point quadrupole (2CLJQ). Additional parameters of the 2CLJQ model are the molecular elongation L and the quadrupole moment Q. The parameters of the molecular models, cf. Table 1, were adjusted to experimental vapor-liquid equilibria in prior work [49].

Series of MD simulations of nucleating vapors were conducted using a version of the **ls**$_1$ program [50]. The simulations were carried out in the canonical ensemble, with a time step between 3 and 7 fs, depending on the system temperature. The cutoff radius r_c was larger than 4.5σ in all simulations. The temperature of the whole system was kept constant by isokinetic scaling.

To follow the kinetics of the phase transition in detail, a criterion which detects clusters of molecules, i.e. the dispersed liquid phase, must be applied to the whole ensemble. In past studies, a considerable number of different cluster criteria were discussed and compared [51, 52, 53, 54, 55]. Those presented by Hill [56] and Stillinger [57] are among the most common ones. They are applied to all pair interactions and the clusters are defined as the connected components of the graph with the molecules as its nodes and edges between the pairs with interactions that fulfill a pair critierion. The Hill energetic criterion is defined by

$$u(r_{ij}) + \frac{m v_{\mathrm{rel}}^2}{2} \;<\; 0, \qquad (25)$$

and the Stillinger geometric criterion by

$$r_{ij} \;<\; r_{\mathrm{gc}}, \qquad (26)$$

where $r_{\mathrm{gc}} = 1.5\sigma$ for the Lennard-Jones fluid. The above definitions distinguish the bulk phases. A hybrid cluster criterion which combines these definitions was consistently observed to select only few clusters with extremely short lifetimes, whereas it reliably detected stable clusters of all sizes. It is defined as follows:

- All molecules i for which the energetic single-molecule criterion

  $$m v_i^2 + \Sigma_{i \neq j} u_{\mathrm{pot}}(r_{ij}) \;<\; 0, \qquad (27)$$

  holds are defined to be *liquid*.

- Two liquid molecules are regarded as *connected* whenever they fulfill the Stillinger criterion. For the 2CLJQ model the maximal connection radius is given by

  $$r_{\mathrm{gc}} \;=\; \frac{3\sigma}{2} + \frac{L}{4}. \qquad (28)$$

- Clusters are determined by covering a graph consisting of these connections with maximal *biconnected components* and eliminating their overlap. Monomeric clusters are regarded as vapor molecules.

Biconnected components are, by definition, subsets of a graph that cannot be separated into two unconnected parts by removing only one vertex. This reflects the idea that a cluster should not consist of several sub-nuclei connected by a single molecule, because structures that do depend on such a connection tend to be extremely unstable.

The Hill energetic criterion favors molecules with a low kinetic energy, and hence leads to artefacts in the cluster temperature, i.e. clusters are observed to be colder than they actually are. This effect carries over to the hybrid criterion. For this reason, temperature data as displayed in Figure 3 (center) were gathered by applying only the geometric and the biconnectivity parts of the hybrid criterion.

The MD program **ls**$_1$ relies on spatial domain decomposition for parallel simulations [50]. The operation of partitioning a very large graph into biconnected components was handled by including the **boost** library [58] which implements Tarjan's linear time algorithm. Figure 1 (center and right) shows that **ls**$_1$, both with and without cluster recognition, scales well on typical clusters of workstations. This permits simulations of volumes $V \approx 10^{-21}\,\mathrm{m}^3$ for a time span of a few nanoseconds with an acceptable computational effort. Thus with the direct approach, which requires at least some stable nuclei to appear, only values $J > 10^{30}/(\mathrm{m}^3\mathrm{s})$ are accessible unless correspondingly larger computational resources are employed.

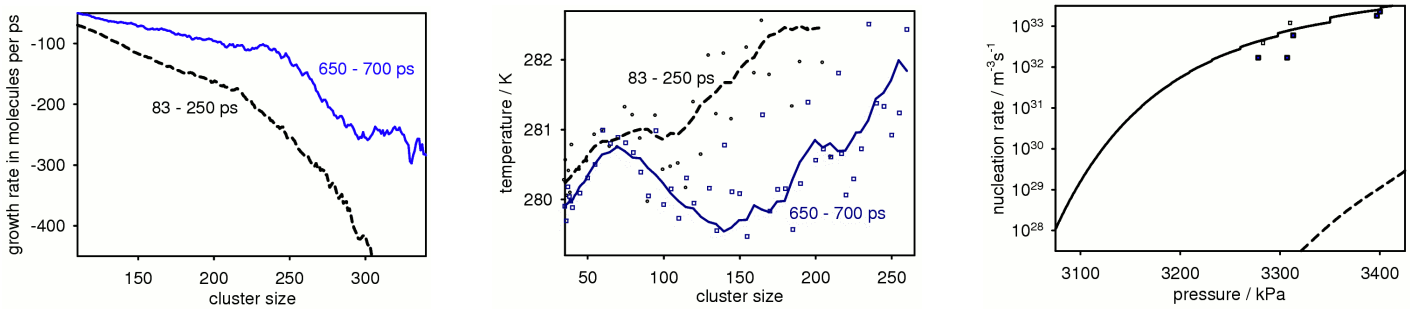

Figure 3: **left** – Cluster net growth rate as a function of cluster size and time in C_2H_6 at 280 K and 2.800 mol/l; **center** – Cluster temperature as a function of cluster size and time in C_2H_6 at 280 K and 2.800 mol/l; data (circles) and running average (- - -) from 83 to 250 ps as well as data (squares) and running average (—) from 650 to 700 ps after the initial state; **right** – Nucleation rate of C_2H_6 at 280 K; small squares: $J(50)$, large squares: $J(75)$ and $J(100)$

4 Simulation results

4.1 Growth rates of single nuclei

Both CNT and the Dillmann-Meier model assume that the properties of clusters with a given size depend only on the temperature and supersaturation of the vapor. Hence, one should expect droplets of the same size generated earlier and later during a simulation run to have, on average, constant temperatures and rates of growth and evaporation.

It is known from MD simulations by Tanumura et al. [59] that this does not necessarily hold in the initial period: the very first clusters of a given size have a higher kinetic energy than those which belong to the actual metastable vapor. This is due to the fact that molecules lose potential energy when they attach to a droplet, which transforms to kinetic energy. The first large clusters have experienced a relatively fast growth process and hence retain more of this latent heat. The present simulations confirm this observation, cf. Figure 3 (center), which shows that the largest existing clusters have a temperature of 282 K and above, while the whole system temperature is fixed at 280 K. The lower curve, collected between 650 and 700 after the simulation onset, exhibits a local maximum of the cluster temperature at a size of about 70 molecules. The temperature of smaller clusters changes comparatively little over simulation time, i.e. with respect to the higher curve, whereas for larger clusters it decreases considerably. The temperature of the clusters with $\iota < 70$ has reached a steady state, but no thermal equilibrium with the vapor, which implies that these clusters are unstable. For $\iota > 70$, no steady state is established and the cluster temperature approaches 280 K. Hence, the local maximum of the temperature plot marks the transition between unstable clusters and stable nano-droplets, i.e. the size of the critical nucleus. It agrees well with the critical size of 78 indicated by CNT, as opposed to the LFK model which predicts $\iota^* = 207$, cf. Table 6.

As an effect which is closely related to the overheating of the dispersed phase, clusters generated early in the condensation process evaporate at a higher rate than those which are generated later, cf. Figure 3 (left). These data were collected during the same simulation as those from Figure 3 (center). Note how the growth rate of clusters is negative for sizes significantly larger than the critical nucleus, where ι^* can be estimated either from the temperature profile any of the theories. This phenomenon was also observed by Yasuoka and Matsumoto [24]. The positive contribution to cluster growth, which is due to

	T [K]	ρ [mol/l]	MFPT J	direct MD $J(10)$
Ar	50.0	0.139	1×10^{31} /(m^{3}s)	5×10^{30} /(m^{3}s)
CH_4	63.6	0.105	1×10^{31} /(m^{3}s)	6×10^{30} /(m^{3}s)

Table 2: Comparison of the nuclation rate from an MFPT indirect analysis according to Wedekind et al. [46] with the value $J(10)$ from another simulation of that system analyzed with the method of Yasuoka and Matsumoto; a single set of values for the LJ fluid is interpreted as both argon and methane

$\mathcal{S}_\rho$	$\mathcal{S}_p$	$\mathcal{S}_\mu$	ι	$J(\iota)$ [m^{-3}s^{-1}]	ι^*(CNT)	J(CNT) [m^{-3}s^{-1}]	ι^*(LFK)	J(LFK) [m^{-3}s^{-1}]
1.694	1.269	1.164	25	1.3×10^{33}	49	1.1×10^{34}	132	4.1×10^{30}
1.694	1.263	1.161	75	$\mathbf{1.8 \times 10^{32}}$	51	$\mathbf{8.0 \times 10^{33}}$	139	2.5×10^{30}
1.694	1.250	1.154	225	$\mathbf{1.5 \times 10^{32}}$	57	$\mathbf{6.6 \times 10^{33}}$	153	$\mathbf{8.7 \times 10^{29}}$
1.769	1.273	1.166	25	2.1×10^{33}	47	1.2×10^{34}	128	6.2×10^{30}
1.769	1.259	1.159	75	$\mathbf{4.0 \times 10^{32}}$	53	$\mathbf{7.6 \times 10^{33}}$	143	1.8×10^{30}
1.769	1.247	1.153	225	$\mathbf{2.7 \times 10^{32}}$	59	$\mathbf{5.2 \times 10^{33}}$	157	$\mathbf{6.7 \times 10^{29}}$

Table 3: Simulation results and theoretical values of nucleation rates for supersaturated methane at 170 K with p_σ= 2328 kPa, ρ_σ= 2.429 mol/l, and γ_0= 2.07 g/s^2; bold values: threshold $\iota > \iota^*$ according to theory

condensation of the vapor phase, remains constant over simulation time. This indicates that while the temperature of clusters with a given size changes, the temporal evolution of the system does not significantly affect their surface area. From the decrease in cluster evaporation over time, it clearly follows that for MD simulations starting from a cluster-free configuration, the first clusters differ significantly from the much larger number of clusters of the same size that appear at a later stage of the process.

Changing rates of evaporation also imply that the critical size can actually vary during a simulation run with a very high supersaturation. For systems at very high supersaturations, it is impossible to observe a metastable vapor phase, because nucleation begins immediately. Such phenomena are only realistic if it is technically possible to increase the supersaturation faster than the vapor phase can produce small clusters.

A magic number effect can be observed for small clusters of both the LJ and the 2CLJQ fluids: the rate of evaporation is comparatively low for clusters with $\iota \in \{8, 11, 14, \ldots, 26\}$ molecules. As opposed to this, clusters with $\iota \in \{4, 9, 12, 15\}$ are detected to have particularly high rates of evaporation. Within this range, 23 and 26, but also 13 and 19, are known as preferred cluster sizes of the LJ fluid [60]. In the present study, the magic numbers may well be a side effect of the biconnectivity requirement of the hybrid cluster criterion. This conclusion is also suggested by the fact that the observed magic numbers do not depend on the employed molecular model.

4.2 Nucleation rates

A nucleation process *at constant pressure* in an infinitely large system occurs, by definition, with the nucleation rate

$$J = \lim_{\iota \to \infty} \lim_{t \to \infty} \frac{d\rho_\iota(t)}{dt}. \tag{29}$$

From molecular simulation in the canonical ensemble, a smoothed $\tilde{\rho}_\iota(t)$, where the statistical noise is reduced, can be constructed from $\rho_\iota(t)$ by averaging over a number of time steps. Such smoothed plots are shown in Figure 2 (left and center). The nucleation rate may then be approximated by the expression

$$J(\iota) = \max_{t > t_0} \frac{d\tilde{\rho}_\iota(t)}{dt}. \tag{30}$$

This approach was introduced by Yasuoka and Matsumoto [24]. The values of $J(\iota)$ are meaningful for all $\iota \geq \iota^*$. However, it has to be taken into account that as the condensation proceeds in a closed system, the number of monomers decreases and the pressure in the vapor is reduced significantly, which causes larger nuclei to be formed at a lower rate, cf. Figure 2 (center).

The present simulation data suggest that, as expected, the values of $J(\iota)$ are similar for values of ι above a certain value, except for cases where the supersaturation decreases significantly, cf. Figures 3 (right) and 4 (left and center) as well as Tables 3, 4, 5, and 6. On the other hand, $J(\iota)$ with very small ι is often significantly elevated, which raises doubts whether results related to $J(6)$, cf. Kraska [27], can lead to reliable conclusions. The nucleation rates are displayed together with pressure values, which were taken in the center of the interval where the plot of $\tilde{\rho}_\iota(t)$ and the linear approximation from which the value of $J(\iota)$ is obtained, roughly agree – for instance, after two nanoseconds in the case of Figure 2 (left).

Wedekind et al. [36] propose an indirect method for the determination of both the nucleation rate and the critical size from simulation data on mean first passage times. This approach consists in fitting the values of $\mathit{\Gamma}_\infty$, x, and ι^* such that Equation (21) agrees optimally with the actual plot of $\mathit{\Gamma}(\iota)$ from an MD simulation. However, Wedekind et al. [47, Figure 4] also note that the size of the critical nucleus determined according to this MFPT based approach can deviate by a factor larger than two from the 'nucleation theorem,'

$$\frac{\partial \ln J}{\partial \ln \mathcal{S}_p} \approx \iota^* + 2, \tag{31}$$

obtained by Oxtoby and Kashchiev [61] in a similar version. That is not necessarily an argument against the method, since the nucleation theorem is known to be valid

$\mathcal{S}_\rho$	$\mathcal{S}_p$	$\mathcal{S}_\mu$	ι	$J(\iota)$ [m^{-3}s^{-1}]	ι^*(CNT)	J(CNT) [m^{-3}s^{-1}]	ι^*(LFK)	J(LFK) [m^{-3}s^{-1}]
2.032	1.61	1.42	50	9.1×10^{31}	58	1.3×10^{32}	80	8.4×10^{29}
2.096	1.63	1.43	25	6.2×10^{31}	54	2.0×10^{32}	75	1.7×10^{30}
2.352	1.70	1.47	25	6.7×10^{32}	44	6.9×10^{32}	59	2.5×10^{31}
2.352	1.69	1.46	100	$\mathbf{1.2 \times 10^{32}}$	46	$\mathbf{5.9 \times 10^{32}}$	61	$\mathbf{1.7 \times 10^{31}}$
2.481	1.72	1.48	25	1.4×10^{33}	42	9.1×10^{32}	55	6.1×10^{31}
2.481	1.70	1.47	100	$\mathbf{2.9 \times 10^{32}}$	44	$\mathbf{6.9 \times 10^{32}}$	59	$\mathbf{2.5 \times 10^{31}}$
2.609	1.73	1.48	25	2.2×10^{33}	41	1.0×10^{33}	54	6.7×10^{31}
2.609	1.70	1.47	100	$\mathbf{7.6 \times 10^{32}}$	44	$\mathbf{6.9 \times 10^{32}}$	59	$\mathbf{2.5 \times 10^{31}}$
2.695	1.71	1.47	200	$\mathbf{8.4 \times 10^{32}}$	43	$\mathbf{8.0 \times 10^{32}}$	57	$\mathbf{3.8 \times 10^{31}}$
2.695	1.70	1.47	500	$\mathbf{4.9 \times 10^{32}}$	44	$\mathbf{6.9 \times 10^{32}}$	59	$\mathbf{2.5 \times 10^{31}}$

Table 4: Simulation results and theoretical values of nucleation rates for supersaturated carbon dioxide at 253 K with p_σ= 1961 kPa, ρ_σ= 1.169 mol/l, and γ_0= 86.2 g/s^2; bold values: threshold $\iota > \iota^*$ according to theory

only for moderate supersaturations [62]. Table 3 compares a new MD simulation, evaluated according to the method of Yasuoka and Matsumoto, with data obtained by Wedekind et al. [46] following the MFPT approach. The value of $J(10)$ is probably larger than J, since nucleation rates of about 10^{30} – 10^{31} usually imply critical sizes $\iota^* \gg 10$. However, $J(10)$ is significantly lower than the MFPT extrapolation.

4.3 Delay of cluster formation

Statistics on the formation delay of ι-clusters are shown in Figure 2 (right). The plots are of the type

$$\nu_\xi(t) \;=\; \max\{\mathrm{n} \in \mathbb{N} \,|\, \Sigma_{(\iota \geq \mathrm{n})}\, \iota\rho_\iota \;\geq\; \xi\rho\}, \qquad (32)$$

with $0 < \xi \leq 1$, i.e. they show the nucleation threshold $\nu_\xi(t)$ passed by a mole fraction ξ of the condensing fluid at the time t.

For instance, after 0.5 ns, $N/16 = 55300$ or more molecules are in clusters with a size $\iota \geq \nu_{1/16}(0.5\mathrm{ns}) = 450$, but the clusters of 451 or more molecules contain less than 55300 molecules. At the same time, the threshold corresponding to $N/1024 = 864$ molecules lies at $\nu_{1/1024}(0.5\mathrm{ns}) = 1519$, i.e. there are at least 864 molecules in clusters with $\iota \geq 1519$, but not in clusters with $\iota \geq 1520$. Thus the plot corresponding to $\nu_{1/1024}(t)$ shows the development of the largest cluster. For that reason, it oscillates more than the other plots.

For $\xi \to 0$, the expected values of $\nu_\xi(t)$ converge by definition towards the inverse function of $\mathit{\Gamma}(\iota)$, since by inverting such a plot the first passage times are obtained. Consider such first passage times from simulations of methane, cf. Figure 4 (right). The data correspond to droplets much larger than the critical nucleus, cf. Table 3. From Equation (22) and (23) it would be expected that the mean first passage time converges according to

$$\lim_{\iota \to \infty} \mathit{\Gamma}(\iota) \;=\; \frac{1}{JV}, \qquad (33)$$

which corresponds to 66 ps for 4.116 mol/l and to 38 ps for 4.298 mol/l, if we accept the values of $J(225)$ determined with the method of Yasuoka and Matsumoto. However, no convergence on such a timescale can be observed, and this is certainly not a matter of the statistical uncertainty of conducting a single simulation. The tendency of the mean first passage time to diverge instead of reaching a plateau can also be observed for data published by Wedekind [45, Figure 4.11 (bottom)].

5 Comparison of theory and simulation

The simulation results for $J(\iota)$ are compared to CNT and LFK in Figures 3 (right) and 4 (left and center) as well as Tables 3, 4, 5, and 6.

The correlation between p, ρ and $\Delta\mu$ at constant T, which is necessary to evaluate the considered models, was obtained from simulations of small supersaturated systems analogous to those described in previous work [63]. The dependence of p on ρ between data points was approximated by a linear fit. The resulting isotherms were used to estimate the density $\rho(p, T)$ of the vapor, which decreases over simulation time, to reflect that with a decreasing supersaturation, nuclei should be expected to emerge at a lower rate – note that the values of ρ shown in the tables correspond to the density of the entire system, not to the remaining vapor. The isotherms were also applied to determine the second virial coefficient for the LFK model according to Equation (14), and the chemical potential difference between the saturated and the supersaturated vapor according to Equation (2). In Tables 3, 4, and 5 the supersaturation with respect to the density, $\mathcal{S}_\rho = \rho/\rho_\sigma(T)$, as well as the pressure are shown together with

$$\mathcal{S}_\mu \;=\; \exp\left(\frac{\mu(p,T) - \mu_\sigma(T)}{kT}\right), \qquad (34)$$

i.e. the supersaturation with respect to the chemical potential, where $\rho_\sigma(T)$ and $\mu_\sigma(T)$ refer to the saturated vapor at the given temperature. Occasionally, the identity $\mathcal{S}_\rho = \mathcal{S}_p = \mathcal{S}_\mu$ is assumed in the literature [8, 14, 45]; in particular, it is used for the derivation of Equation (31), where $\mathcal{S}_p$ replaces the more accurate $\mathcal{S}_\mu$. However, near the spinodal this is always a bad approximation, since $\partial p/\partial\rho \to 0$ holds there by definition.

$\mathcal{S}_\rho$	$\mathcal{S}_p$	$\mathcal{S}_\mu$	ι	$J(\iota)$ [$\mathrm{m^{-3}s^{-1}}$]	ι^*(CNT)	J(CNT) [$\mathrm{m^{-3}s^{-1}}$]	ι^*(LFK)	J(LFK) [$\mathrm{m^{-3}s^{-1}}$]
1.079	1.077	1.047	25	3.3×10^{33}	629	2.3×10^{29}	1390	2.7×10^{15}
1.079	1.078	1.047	50	6.5×10^{32}	607	3.1×10^{29}	1350	5.7×10^{15}
1.177	1.112	1.067	50	4.8×10^{32}	222	1.5×10^{32}	596	2.4×10^{23}
1.177	1.111	1.066	75	1.1×10^{32}	228	1.4×10^{32}	608	1.7×10^{23}
1.238	1.133	1.078	50	2.4×10^{33}	140	7.7×10^{32}	416	6.2×10^{25}
1.238	1.135	1.079	75	1.4×10^{33}	135	8.3×10^{32}	403	1.0×10^{26}

Table 5: Simulation results and theoretical values of nucleation rates for supersaturated carbon dioxide at 285 K with p_σ= 4712 kPa, ρ_σ= 3.270 mol/l, and γ_0= 24.5 g/s^2; for all values the threshold ι is lower than ι^* according to theory

	T [K]	ρ $\left[\frac{\mathrm{mol}}{\mathrm{l}}\right]$	p [kPa]	ι	$J(\iota)$ $\left[\frac{1}{\mathrm{m^3 s}}\right]$	ι^*(CNT)	J(CNT) $\left[\frac{1}{\mathrm{m^3 s}}\right]$	ι^*(LFK)	J(LFK) $\left[\frac{1}{\mathrm{m^3 s}}\right]$
$\mathbf{CH_4}$	106.0	0.758	503	25	$\mathbf{1.8 \times 10^{32}}$	22	$\mathbf{1.6 \times 10^{29}}$	16	$\mathbf{9.9 \times 10^{31}}$
	114.0	0.851	616	75	$\mathbf{2.7 \times 10^{31}}$	23	$\mathbf{2.1 \times 10^{30}}$	19	$\mathbf{5.7 \times 10^{31}}$
	114.0	0.851	614	150	$\mathbf{2.8 \times 10^{31}}$	23	$\mathbf{2.0 \times 10^{30}}$	19	$\mathbf{5.4 \times 10^{31}}$
	114.0	0.925	641	75	$\mathbf{5.8 \times 10^{31}}$	22	$\mathbf{4.5 \times 10^{30}}$	18	$\mathbf{1.2 \times 10^{32}}$
	114.0	0.925	629	150	$\mathbf{5.5 \times 10^{31}}$	23	$\mathbf{3.2 \times 10^{30}}$	18	$\mathbf{8.5 \times 10^{31}}$
	130.0	1.432	1022	700	$\mathbf{2.1 \times 10^{31}}$	31	$\mathbf{3.2 \times 10^{31}}$	31	$\mathbf{3.1 \times 10^{31}}$
	130.0	1.606	1095	75	$\mathbf{6.2 \times 10^{32}}$	26	$\mathbf{1.3 \times 10^{32}}$	26	$\mathbf{1.7 \times 10^{32}}$
	130.0	1.693	1148	25	$\mathbf{2.5 \times 10^{33}}$	24	$\mathbf{3.2 \times 10^{32}}$	22	$\mathbf{6.2 \times 10^{32}}$
	130.0	1.780	1167	25	$\mathbf{4.0 \times 10^{33}}$	23	$\mathbf{4.1 \times 10^{32}}$	21	$\mathbf{7.8 \times 10^{32}}$
$\mathbf{C_2H_6}$	176.5	0.385	455	25	$\mathbf{1.3 \times 10^{31}}$	16	$\mathbf{4.5 \times 10^{30}}$	15	$\mathbf{2.7 \times 10^{31}}$
	176.5	0.400	467	25	$\mathbf{2.0 \times 10^{31}}$	16	$\mathbf{6.4 \times 10^{30}}$	14	$\mathbf{3.9 \times 10^{31}}$
	280.0	2.470	3283	50	3.9×10^{32}	131	4.6×10^{32}	322	2.8×10^{26}
	280.0	2.470	3278	75	1.7×10^{32}	135	4.2×10^{32}	329	2.0×10^{26}
	280.0	2.550	3307	100	1.7×10^{32}	116	7.7×10^{32}	290	1.2×10^{27}
	280.0	2.800	3397	100	$\mathbf{1.8 \times 10^{33}}$	78	$\mathbf{2.5 \times 10^{33}}$	207	9.0×10^{28}
	280.0	2.950	3430	75	$\mathbf{3.3 \times 10^{33}}$	68	$\mathbf{3.6 \times 10^{33}}$	186	3.1×10^{29}
	280.0	2.950	3427	100	$\mathbf{1.9 \times 10^{33}}$	69	$\mathbf{3.5 \times 10^{33}}$	188	2.8×10^{29}
$\mathbf{CO_2}$	237.0	1.700	2283	75	$\mathbf{1.1 \times 10^{31}}$	50	$\mathbf{9.4 \times 10^{30}}$	57	$\mathbf{7.7 \times 10^{29}}$
	237.0	1.750	2317	75	$\mathbf{1.8 \times 10^{31}}$	48	$\mathbf{1.6 \times 10^{31}}$	55	$\mathbf{1.3 \times 10^{30}}$
	237.0	1.850	2322	300	$\mathbf{9.6 \times 10^{31}}$	47	$\mathbf{1.7 \times 10^{31}}$	54	$\mathbf{1.5 \times 10^{30}}$
	237.0	2.000	2333	300	$\mathbf{2.3 \times 10^{32}}$	46	$\mathbf{2.0 \times 10^{31}}$	53	$\mathbf{2.0 \times 10^{30}}$
	237.0	2.450	2499	75	$\mathbf{4.7 \times 10^{33}}$	37	$\mathbf{1.4 \times 10^{32}}$	40	$\mathbf{4.2 \times 10^{31}}$
	269.0	3.120	4142	25	4.7×10^{33}	81	4.7×10^{32}	147	6.7×10^{28}
	269.0	3.120	4131	75	3.6×10^{32}	83	4.2×10^{32}	150	5.1×10^{28}
	269.0	3.800	4350	50	6.5×10^{33}	54	2.6×10^{33}	99	6.7×10^{30}
	269.0	3.800	4343	75	$\mathbf{4.1 \times 10^{33}}$	55	$\mathbf{2.5 \times 10^{33}}$	100	5.8×10^{30}

Table 6: Simulation results and theoretical values of nucleation rates for supersaturated methane, ethane, and carbon dioxide; bold values: threshold $\iota > \iota^*$ according to theory

Values of $J(\iota)$ determined with the method of Yasuoka and Matsumoto are only significant for $\iota > \iota^*$. Since the size of the critical nucleus can not be obtained by means of this method, the theories are checked against their own predictions of ι^*: if the theoretical value of ι^* is smaller than the threshold used to evaluate the MD simulation, then simulation and theory should be expected to agree. Such data are directly comparable – they correspond to the highlighted values in Tables 3, 4, 5, and 6.

The values collected for the quadrupolar fluids show an eccellent agreement with CNT: all directly comparable nucleation rates agree within one order of magnitude. For methane, CNT significantly underestimates the nucleation rate at 106 K and overestimates it at 170 K. The predictions of J based on the LFK model are generally too low for carbon dioxide, with an error between one and two orders of magnitude in the directly comparable cases. However, LFK predicts the nucleation rate accurately for methane at 106, 114, and 130 K as well as for ethane at 176.5 K.

Both theories are observed to deviate by about three orders of magnitude from certain directly comparable $J(\iota)$ values: for methane at 106 K and 503 kPa, the method of Yasuoka and Matsumoto yields $J(25) = 1.8 \times 10^{32}/(\mathrm{m^3 s})$, while CNT predicts $J = 1.6 \times 10^{29}/(\mathrm{m^3 s})$, cf. Table 6. For methane at 170 K and $\mathcal{S}_p = 1.247$, cf. Table 3, the nucleation rate according to the LFK model is $J = 6.7 \times 10^{29}/(\mathrm{m^3 s})$ as opposed to $J(225) = 2.7 \times 10^{32}/(\mathrm{m^3 s})$, obtained from an MD simulation.

Conclusion. Simulations of large nucleating systems in the canonical ensemble were conducted and analyzed according to the method of Yasuoka and Matsumoto. The observation that cluster temperature, for a given size, decreases over time, casts doubt on the MFPT indirect approach of nucleation analysis which considers only the first

clusters of a given size and extracts an estimate for the steady-state nucleation rate from their delay of formation. It was shown that the decreasing amount of latent heat retained by the dispersed phase leads to a relevant change of the cluster growth over time. The critical nucleus size determined from a temperature profile of ethane clusters at a high temperature ($0.9\,T_c$) confirms CNT, whereas the LFK model overestimates this value by a factor of three. Nucleation rates from both CNT and LFK were observed to agree within three orders of magnitude with those simulation results that can be compared directly to the theories. In particular, CNT shows almost no deviation for ethane and carbon dioxide. The LFK model consistently predicts extremely low nucleation rates at high temperatures, but agrees very well with the nucleation rates of methane and ethane at low temperatures.

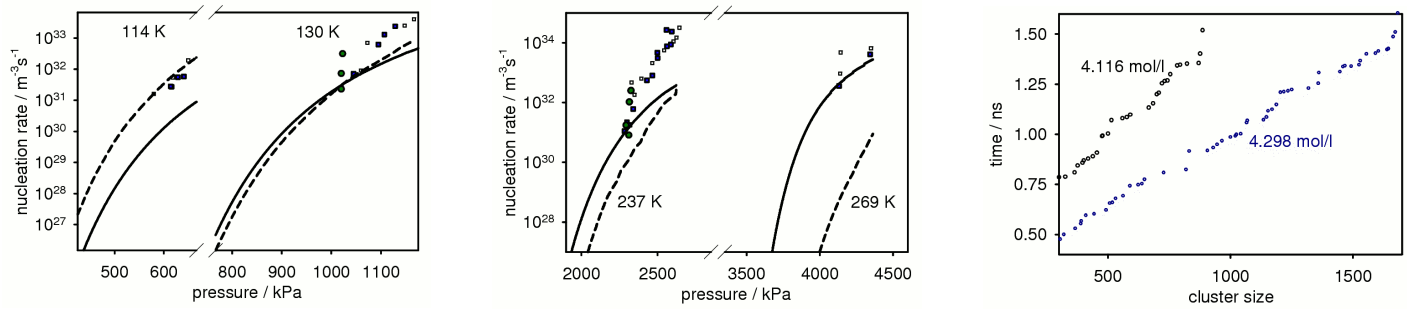

Figure 4: **left** – Nucleation rate of CH_4 at 106, 114, and 130 K; small squares: $J(25)$, large squares: $J(75)$ and $J(150)$, circles: $J(225)$ and $J(700)$; **center** – Nucleation rate of CO_2 at 237 and 269 K; small squares: $J(25)$ and $J(50)$, large squares: $J(75)$, circles: $J(300)$; **right** – First passage time of clusters in CH_4 at 170 K with $N = 250000$

Acknowledgment. The authors thank Ralf Kible, Nicolas Schmidt, and Jonathan Walter for fruitful discussions, Deutsche Forschungsgemeinschaft for funding Sonderforschungsbereich 716 'Dynamic Simulation of Systems with Large Numbers of Particles', Landesstiftung Baden-Württemberg for funding project 688 'Massiv parallele molekulare Simulation und Visualisierung der Keimbildung in Mischungen für skalenübergreifende Modelle,' as well as the Simulation of Large Systems group at the Institute of Parallel and Distributed Systems and the Numerics for Supercomputers group at the Institute of Applied Analysis and Numerical Simulation, Universität Stuttgart, for providing access to the *mozart* cluster.

References

[1] J. W. Gibbs, *Collected Works. Vol 1. Thermodynamics.* New York: Longmans-Green, 1928.

[2] M. Volmer and A. Weber *Z. Phys. Chem.*, vol. 119, pp. 277–301, 1926.

[3] L. Farkas *Z. Phys. Chem.*, vol. 125, p. 326, 1927.

[4] C. T. R. Wilson *Phil. Trans. A*, vol. 189, p. 265, 1897.

[5] C. F. Powell *Proc. Roy. Soc. A*, vol. 119, p. 553, 1928.

[6] J. A. Fisk, M. M. Rudek, J. L. Katz, D. Beiersdorf, and H. Uchtmann *Atm. Res.*, vol. 46, p. 211, 1998.

[7] J. D. Gunton *J. Stat. Phys.*, vol. 95, no. 5/6, pp. 903–923, 1999.

[8] I. J. Ford *Proc. Inst. Mech. Eng. C: J. Mech. Eng. Sci.*, vol. 218, pp. 883–899, 2004.

[9] B. J. Alder and T. E. Wainwright *J. Chem. Phys.*, vol. 27, pp. 1208–1209, 1957.

[10] D. J. McGinty *J. Chem. Phys.*, vol. 58, no. 11, pp. 4733–4742, 1973.

[11] M. Rao, B. J. Berne, and M. H. Kalos *J. Chem. Phys.*, vol. 68, no. 4, pp. 1325–1336, 1978.

[12] D. I. Zhukovitskii *J. Chem. Phys.*, vol. 103, no. 21, pp. 9401–9407, 1995.

[13] K. Laasonen, S. Wonczak, R. Strey, and A. Laaksonen *J. Chem. Phys.*, vol. 113, no. 21, pp. 9741–9747, 2000.

[14] J. H. ter Horst and D. Kashchiev *J. Chem. Phys.*, vol. 119, no. 4, pp. 2241–2246, 2003.

[15] J. C. Barrett *J. Chem. Phys.*, vol. 126, p. 074312, 2007.

[16] M. Salonen, I. Napari, and H. Vehkamäki *Mol. Sim.*, vol. 33, no. 3, pp. 245–251, 2007.

[17] R. J. Allen, P. B. Warren, and P. R. ten Wolde *Phys. Rev. Lett.*, vol. 94, p. 018104, 2005.

[18] F. Trudu, D. Donadio, and M. Parrinello *Phys. Rev. Lett.*, vol. 97, p. 105701, 2006.

[19] T. S. van Erp, D. Moroni, and P. G. Bolhuis *J. Chem. Phys.*, vol. 118, pp. 7762–7774, Mai 2003.

[20] H. Vehkamäki and I. J. Ford *J. Chem. Phys.*, vol. 112, no. 9, pp. 4193–4202, 2000.

[21] A. V. Neimark and A. Vishnyakov *J. Phys. Chem. B*, vol. 109, no. 12, pp. 5962–5976, 2005.

[22] P. Bhimalapuram, S. Chakrabarty, and B. Bagchi *Phys. Rev. Lett.*, vol. 98, p. 206104, 2007.

[23] J. Merikanto, E. Zapadinsky, A. Lauri, and H. Vehkamäki *Phys. Rev. Lett.*, vol. 98, p. 145702, 2007.

[24] K. Yasuoka and M. Matsumoto *J. Chem. Phys.*, vol. 109, no. 19, pp. 8451–8470, 1998.

[25] P. Krasnochtchekov, K. Albe, Y. Ashkenazy, and R. S. Averback *J. Chem. Phys.*, vol. 123, p. 154314, 2005.

[26] K. K. Tanaka, K. Kawamura, H. Tanaka, and K. Nakazawa *J. Chem. Phys.*, vol. 122, p. 184514, 2005.

[27] T. Kraska *J. Chem. Phys.*, vol. 124, p. 054507, 2006.

[28] N. Lümmen and T. Kraska *Eur. Phys. J. D*, vol. 41, no. 2, pp. 247–260, 2007.

[29] K. Iland, *Experimente zur homogenen Keimbildung von Argon und Stickstoff*. PhD thesis, University of Cologne, 2004.

[30] D. W. Oxtoby *J. Phys. Cond. Mat.*, vol. 4, no. 38, pp. 7627–7650, 1992.

[31] D. W. Oxtoby *Acc. Chem. Res.*, vol. 31, no. 2, pp. 91–97, 1998.

[32] A. Fladerer and R. Strey *J. Chem. Phys.*, vol. 124, p. 164710, 2006.

[33] A. Dillmann and G. E. A. Meier *J. Chem. Phys.*, vol. 94, no. 5, pp. 3872–3884, 1990.

[34] A. Laaksonen, I. J. Ford, and M. Kulmala *Phys. Rev. E*, vol. 49, no. 6, pp. 5517–5524, 1994.

[35] L. S. Bartell and D. T. Wu *J. Chem. Phys.*, vol. 125, p. 194503, 2006.

[36] J. Wedekind, R. Strey, and D. Reguera *J. Chem. Phys.*, vol. 126, p. 134103, 2007.

[37] R. Becker and W. Döring *Ann. Phys.*, vol. 24, no. 8, pp. 719–752, 1935.

[38] Y. B. Zel'dovich *J. Exp. Theor. Phys.*, vol. 12, p. 525, 1942. In Russian.

[39] J. Feder, K. C. Russell, J. Lothe, and G. M. Pound *Adv. Phys.*, vol. 15, no. 1, pp. 111–178, 1966.

[40] D. Kashchiev, *Nucleation. Basic Theory with Applications*. Oxford: Butterworth-Heinemann, 2000. ISBN 0-7506-4682.

[41] H. Vehkamäki, *Classical Nucleation Theory in Multicomponent Systems*. Berlin – Heidelberg – New York: Springer, 2006. ISBN 3-540-29213-6.

[42] J. P. Hirth and G. M. Pound *Prog. Mater. Sci.*, vol. 11, p. 1, 1963.

[43] M. E. Fisher *Physics*, vol. 3, p. 255, 1967.

[44] I. J. Ford, A. Laaksonen, and M. Kulmala *J. Chem. Phys.*, vol. 99, no. 1, pp. 764–765, 1993.

[45] J. Wedekind, *Nano-Droplets at Birth – Computer Experiments on Gas Phase Nucleation*. PhD thesis, University of Cologne, 2006.

[46] J. Wedekind, D. Reguera, and R. Strey *J. Chem. Phys.*, vol. 125, p. 214505, 2006.

[47] J. Wedekind, J. Wölk, D. Reguera, and R. Strey *J. Chem. Phys.*, vol. 127, p. 154515, 2007.

[48] L. Zhang, Q. An, Y. Xie, Z. Sun, and S.-N. Luo *J. Chem. Phys.*, vol. 127, no. 164503, 2007.

[49] J. Vrabec, J. Stoll, and H. Hasse *J. Phys. Chem. B*, vol. 105, no. 48, pp. 12126–12133, 2001.

[50] M. Bernreuther and J. Vrabec in *High Performance Computing on Vector Systems*, (Springer, Berlin - Heidelberg - New York), pp. 187–195, 2006. ISBN 3-540-29124-5.

[51] R. Badahur and R. B. McClurg *J. Phys. Chem. B*, vol. 105, no. 47, pp. 11893–11900, 2001.

[52] J. C. Barrett *J. Chem. Phys.*, vol. 116, no. 20, pp. 8856–8862, 2002.

[53] N. Sator *Phys. Rep.*, vol. 376, no. 1, pp. 1–39, 2003.

[54] S. Grottel, G. Reina, J. Vrabec, and T. Ertl *IEEE Trans. Vis. Comp. Graph.*, vol. 13, no. 6, pp. 1624–1631, 2007.

[55] J. Wedekind and D. Reguera *J. Chem. Phys.*, vol. 127, p. 154516, 2007.

[56] T. L. Hill *J. Chem. Phys.*, vol. 23, no. 4, pp. 617–622, 1955.

[57] F. H. Stillinger *J. Chem. Phys.*, vol. 38, no. 7, pp. 1486–1494, 1963.

[58] J. G. Siek, L.-Q. Lee, and A. Lumsdaine, *The Boost Graph Library: User Guide and Reference Manual*. Amsterdam: Addison-Wesley Longman, 2001. ISBN 0-201-72914-8.

[59] S. Tanumura, K. Yasuoka, and T. Ebisuzaki *J. Chem. Phys.*, vol. 112, pp. 3812–3819, Februar 2000.

[60] T. Ikeshoji, B. Hafskjold, Y. Hashi, and Y. Kawazoe *Phys. Rev. Lett.*, vol. 76, no. 11, pp. 1792–1795, 1996.

[61] D. W. Oxtoby and D. Kashchiev *J. Chem. Phys.*, vol. 100, no. 10, pp. 7665–7671, 1994.

[62] J. W. P. Schmelzer *J. Coll. Interf. Sci.*, vol. 242, no. 2, pp. 354–372, 2001.

[63] A. Linhart, C.-C. Chen, J. Vrabec, and H. Hasse *J. Chem. Phys.*, vol. 122, p. 144506, 2005.